Multihole water oxidation catalysis on haematite photoanodes revealed by operando spectroelectrochemistry and DFT

Camilo A. Mesa [1,8], Laia Francàs[1,8], Ke R. Yang [2], Pablo Garrido-Barros [2,3], Ernest Pastor [1], Yimeng Ma [1], Andreas Kafizas [1,4], Timothy E. Rosser[5], Matthew T. Mayer [6,7], Erwin Reisner [5], Michael Grätzel[6], Victor S. Batista [2]* and James R. Durrant [1]*

Water oxidation is the key kinetic bottleneck of photoelectrochemical devices for fuel synthesis. Despite advances in the identification of intermediates, elucidating the catalytic mechanism of this multi-redox reaction on metal–oxide photoanodes remains a significant experimental and theoretical challenge. Here, we report an experimental analysis of water oxidation kinetics on four widely studied metal oxides, focusing particularly on haematite. We observe that haematite is able to access a reaction mechanism that is third order in surface-hole density, which is assigned to equilibration between three surface holes and M(OH)–O–M(OH) sites. This reaction exhibits low activation energy ($E_a \approx 60\,meV$). Density functional theory is used to determine the energetics of charge accumulation and O–O bond formation on a model haematite (110) surface. The proposed mechanism shows parallels with the function of the oxygen evolving complex of photosystem II, and provides new insights into the mechanism of heterogeneous water oxidation on a metal oxide surface.

The light-driven oxidation of water by photosystem II (PS II) is one of the most remarkable catalytic reactions in biology. It provides the reducing electrons for photosynthetic carbon dioxide reduction and releases molecular oxygen, which has generated our aerobic atmosphere. Natural photosynthesis is widely regarded as an inspiration behind the development of artificial photosynthetic systems to harness sunlight and split water into molecular oxygen and hydrogen, or reduce carbon dioxide to carbon-based molecular fuels[1–4]. However, it is often unclear whether natural photosynthetic systems exhibit molecular-scale blueprints and mechanisms, which can help guide the development of artificial systems. So far, most studies of heterogeneous and homogeneous chemical water oxidation have focused on optimizing catalytic turnover frequencies and minimizing overpotentials, or long-term stabilities[5–9]. Mechanistic studies of heterogeneous water oxidation have focused particularly on the identification of reaction intermediates[10]. In the present study, we take an alternative approach by employing an experimental rate law analysis of water oxidation on metal oxide surfaces under a range of conditions, and we complement these kinetic studies with density functional theory (DFT) calculations of a simple molecular analogue for one of these oxides to propose a model for water oxidation on such surfaces.

In electrocatalytic systems, the kinetics of catalysis are often probed from analyses of current/potential (J/V) characteristics, often referred to, for metallic electrodes or defect-free semiconductors (that is, with sharp band edges), as Tafel analyses[11]. However, for non-ideal electrodes, such as semiconductors with multiple redox states and/or non-ideal densities of conduction/valence band states, the interpretation of such J/V data is more complex. The rate of reaction in semiconductor electrodes is often primarily determined by the densities of surface conduction band electrons (valence band holes) or of reduced (oxidized) states of the catalyst[12]. However, for non-ideal semiconductors, these densities are often difficult to determine from J/V analyses alone. For photoelectro-catalytic systems, determination of these densities from J/V data is further complicated by the quasi-Fermi level splitting induced by light. As such, for many (photo)electrocatalytic systems, determination of rate laws for multi-redox reactions is a non-trivial challenge, with only limited studies reported in the literature so far[13]. Similarly, theoretical calculations have typically not addressed the dependence of the reaction rate on surface charge density.

We have recently demonstrated, for both electrocatalytic and photoelectrocatalytic systems, that optical spectroscopy can provide a direct measurement of the densities of the states driving catalysis under operating conditions, and have employed this approach to elucidate rate laws for water and methanol oxidation and proton reduction on different (photo)electrocatalytic surfaces[14–16]. In the present study, we employ this experimental approach to determine the dependence of the water oxidation rate constant upon temperature, pH and H/D exchange for haematite (α-Fe$_2$O$_3$) photoelectrodes, thus providing key experimental data on the underlying reaction mechanism (for details of the methods see Supplementary Information). This experimental approach combines a transient optical absorption assay of surface hole accumulation (h_s^+) (see Supplementary Fig. 1 for typical absorption spectra of these holes on haematite; we note these surface holes are likely to be relatively

[1]Molecular Sciences Research Hub and Centre for Plastic Electronics, Imperial College London, London, UK. [2]Department of Chemistry and Energy Sciences Institute, Yale University, New Haven, CT, USA. [3]Institute of Chemical Research of Catalonia (ICIQ), Tarragona, Spain. [4]The Grantham Institute, Imperial College London, London, UK. [5]Christian Doppler Laboratory for Sustainable SynGas Chemistry, Department of Chemistry, University of Cambridge, Cambridge, UK. [6]Institut des Sciences et Ingénierie Chimiques, Ecole Polytechnique Fédérale de Lausanne, Lausanne, Switzerland. [7]Helmholtz-Zentrum Berlin für Materialien und Energie GmbH, Berlin, Germany. [8]These authors contributed equally: Camilo A. Mesa, Laia Francàs. *e-mail: Victor.batista@yale.edu; j.durrant@imperial.ac.uk
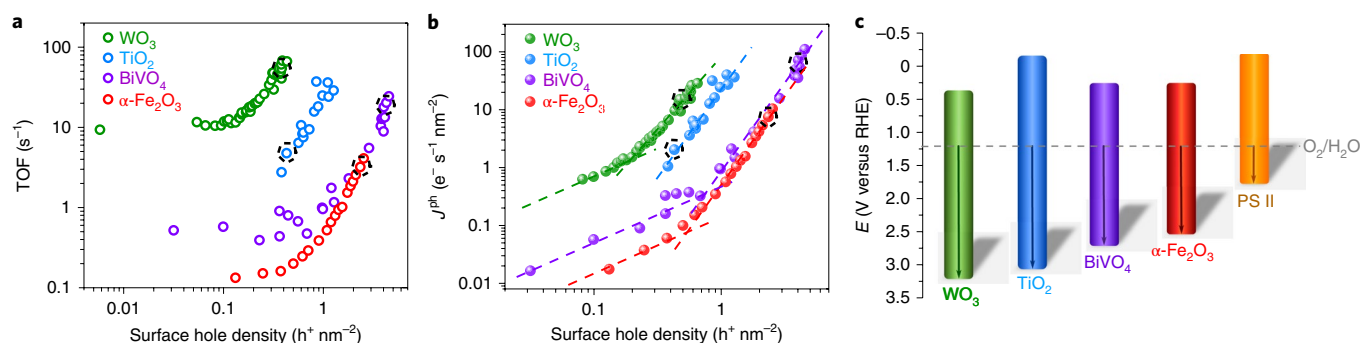
Fig. 1 | Kinetic analysis of the water oxidation reaction on metal oxide photoanodes. a, Chart showing log/log plots of the TOFs for hole transfer to the electrolyte corresponding to water oxidation as a function of surface hole density, measured at fixed anodic bias for four metal oxide photoanodes. The black dashed circles indicate ~1 sun irradiation conditions. **b**, Equivalent data plotted as rate of reaction versus surface hole density. The α-Fe$_2$O$_3$, TiO$_2$ and BiVO$_4$ plots are adapted from previously published data[16–18], ACS. The dashed lines correspond to fits to the rate law (equation (1)). Conditions: WO$_3$, diffuse reflectance system ($\alpha = 1$, $\alpha = 2.5$), pH 3, applied potential 1.4 V versus reversible hydrogen electrode (RHE); BiVO$_4$, transmittance system ($\alpha = 1$, $\alpha = 3$), pH 7 at 1.7 V versus RHE[17]; α-Fe$_2$O$_3$, transmittance system ($\alpha = 1$, $\alpha = 3$), pH 13 at 1.5 V versus RHE[16]; TiO$_2$, transmittance system ($\alpha = 3$) pH 13 at 1.5 V versus RHE[18]. α corresponds to the gradient (dashed lines). In all cases 365 nm LED irradiation was used from 0.5% to 300% of 1 sun and measurements were performed at 25 °C. **c**, Schematic of the VBE energy relative to the H$_2$O oxidation redox potential (1.23 V versus RHE) of the metal oxides discussed in this work, including the equivalent PSII energy levels for reference.

localized, with energies near the valence band edge (VBE))[16–19] with a photoelectrochemical assay of the flux of water oxidation (J^{ph}), which allows us to determine the rate law (equation (1)) on such photoelectrodes:

$$J^{ph} = k_{WO} \cdot (h_s^+)^{\alpha} \qquad (1)$$

where α is the order of the reaction with respect to the hole density and k_{WO} is the corresponding water oxidation rate constant. For the studies reported herein, data were collected under strong anodic bias (to supress surface recombination losses), as a function of light irradiation intensity, in a three-electrode photoelectrochemical cell. Data were collected after irradiation with a 365 nm light-emitting diode (LED) light pulse for 5 s, long enough to reach approximately steady-state conditions for both the surface hole and photocurrent densities[16–18]. The complete optical and electrochemical dataset is available at http://zenodo.org with the identifier 10.5281/zenodo.851635. Our previous kinetic studies have demonstrated that only holes localized in the space charge layer have sufficiently long lifetimes to contribute to the quasi-steady-state conditions employed, and herein we take advantage of the fact that our optical assay is sensitive only to these surface holes[16,20].

Results and discussion

We start by making a quantitative comparison of the dependence of the water oxidation kinetics on the density of photogenerated charge carriers on haematite (α-Fe$_2$O$_3$) and on three other photoanodes: titanium dioxide (TiO$_2$), bismuth vanadate (BiVO$_4$) and tungsten oxide (WO$_3$), as shown in Fig. 1a (for α-Fe$_2$O$_3$, TiO$_2$ and BiVO$_4$; refs. [16–18]; see Supplementary Figs. 2 and 3 for optical and electrochemical characterization). These data are plotted as log/log plots of turnover frequency (TOF) versus surface hole density (h_s^+) (where the TOF is determined from the inverse of the hole transfer time constant; oxygen release TOFs would be fourfold slower). We note that the surface hole density can be considered most simply as a measure of how close the hole quasi-Fermi level approaches the valence band maximum at the surface, with a higher hole density corresponding to a greater free energy driving water oxidation. All the oxides studied here have been shown to have promising activity for water oxidation under solar irradiation and modest anodic bias and, with the exception of WO$_3$, near unity Faradaic efficiencies[21]. Unlike PS II, their valence band maxima are all relatively

deep, providing large energy offsets for water oxidation by valence band holes, as illustrated in Fig. 1c. In particular, we have previously reported that the rate of water oxidation increases with the third power of the surface hole density under 1 sun irradiation on α-Fe$_2$O$_3$, BiVO$_4$ and TiO$_2$ (refs. [16–18]), suggesting the co-operative function of three surface holes in the rate determining step (RDS) of the reaction. Further data are included herein for WO$_3$ photoanodes (see Supplementary Figs. 4 and 5 for WO$_3$ details). Also shown in Fig. 1b are the same data plotted more conventionally, as water oxidation flux versus surface hole density.

Figure 1a shows that as the surface hole density is increased, the TOF is initially constant, and then increases, corresponding to a transition from a first-order reaction at low surface hole densities to a faster, higher, circa third-order reaction at higher hole densities, with the latter dominating under 1 sun irradiation. We note that the transition from first to third order is not always quantitative. WO$_3$ photoanodes actually fit best to a 2.5 order at high hole densities, showing non-unity Faradaic efficiency for water oxidation[22]. For TiO$_2$ photoanodes, the first-order regime could not be resolved, and at neutral and acidic pH, we observe second-order behaviour[18]. As we have discussed previously, this unexpected biphasic behaviour suggests distinct reaction mechanisms at different surface hole densities[16,17]. We note that different rate law data have been reported recently for haematite based on J/V impedance data, as discussed further in the Supplementary Information, page 8[23]. The TOFs plotted in Fig. 1a range from 0.125 s^{-1} for α-Fe$_2$O$_3$ at low hole densities to 60 s^{-1} for WO$_3$ at high hole densities. These values are between one to two orders of magnitude slower than that for the oxygen evolving centre (OEC) in PS II[24], but are comparable to many homogeneous and heterogeneous chemical water oxidation catalysts[2,21]. It is apparent from this plot that the TOFs (and therefore rate constants) for water oxidation correlate with the VBEs of these oxides shown in Fig. 1c. α-Fe$_2$O$_3$ exhibits the slowest kinetics and least oxidizing VBE, while WO$_3$ exhibits the fastest kinetics and deepest VBE. More quantitatively, we observe that an increase in the VBE of 0.7 V results in a 150-fold increase in the water oxidation rate constant. Faster water oxidation kinetics can be expected to reduce losses due to kinetic competition with surface (or 'back electron hole') recombination. The variation in water oxidation kinetics we observe in Fig. 1a between these metal oxides is therefore likely to be a key reason why it is easier to achieve photocurrent onset potentials closer to the flat band for WO$_3$
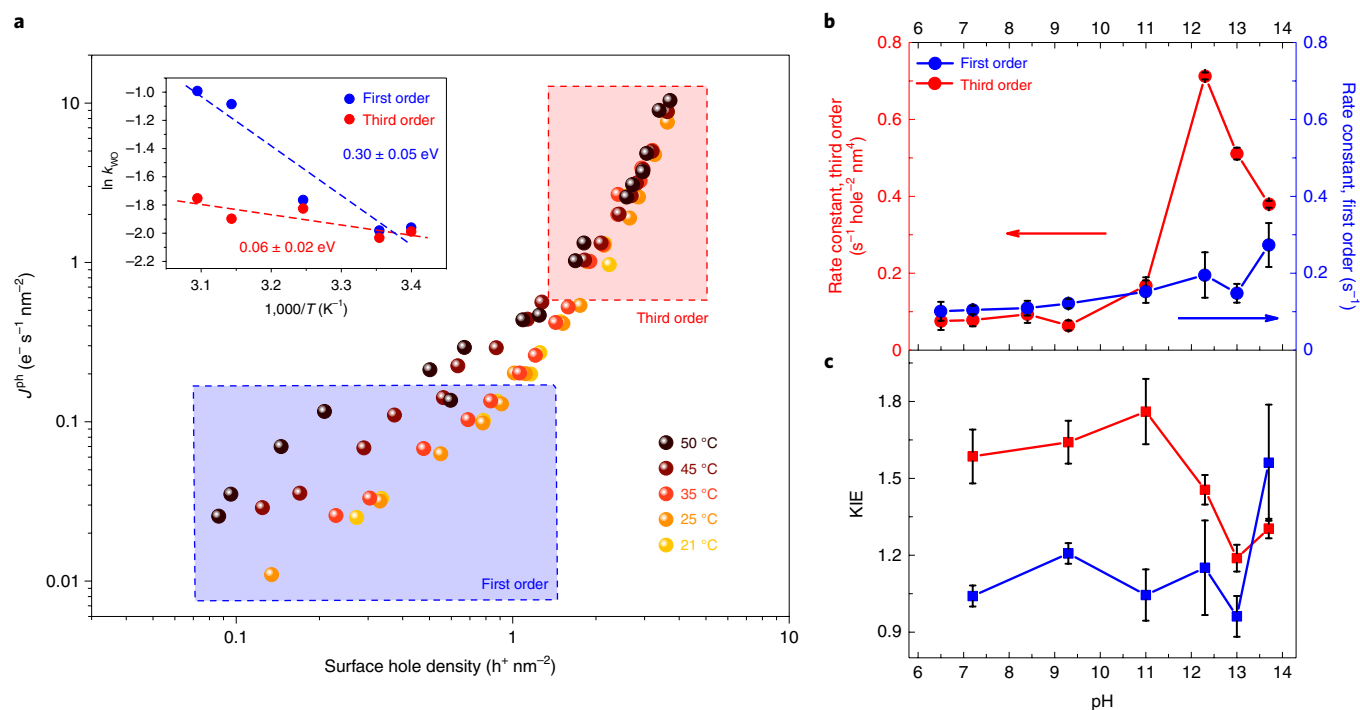
Fig. 2 | Mechanistic analyses of water oxidation on α-Fe₂O₃. a, Rate law analyses as for Fig. 1b, but at different temperatures (21–50 °C). The inset shows an Arrhenius plot of water oxidation rate constant k_{WO} for both the first- and third-order regimes. The slopes (dashed lines) indicate the activation energies of the RDSs, suggesting the catalytic effect of hole accumulation on α-Fe₂O₃. **b**, Plots of the pH dependence of the rate constants of the first- and third-order regimes. **c**, Comparison of the kinetic isotope effect when H_2O is replaced by D_2O at different pH values for the third- (red) and first-order (blue) regimes, exhibiting no cleavage of O–H bonds at the RDSs. In **b** and **c**, error bars represent the s.d. of linear fits of the logarithmic form of equation (1) to the full data sets shown in Supplementary Fig. 8a,b.

(ref. [25]) and TiO₂ (ref. [26]) compared to BiVO₄ (ref. [27]) and α-Fe₂O₃ (Supplementary Fig. 3).

We note that the surface hole densities in Fig. 1a range between 0.5 and 4 h⁺ nm⁻², one to two orders of magnitude higher than the densities of surface defect states typically reported for such oxides[28,29], suggesting that any water oxidation proceeding from such defect states is unlikely to contribute significantly to the data reported herein. We emphasize that this analysis contrasts with Tafel analyses of metallic electrocatalysts, where the applied potential increases the energy of states driving catalysis, by directly measuring the density of reactive species (h_s^+) independently of their dependence on the applied potential. This molecular viewpoint is consistent with surface holes on such oxides being relatively localized states[30], such that their enthalpies can be considered to be, to a first approximation, independent of surface hole density. We also emphasize that our approach can be considered more analogous to that employed for electrochemically driven molecular catalysis, as studied in catalytic Tafel plots. We note that analysis of reaction rates versus the actual driving force of the accumulated redox species (considering the energetics of valence band tail states) would further advance our understanding of these photoelectrochemical systems.

Experimental mechanistic studies of water oxidation on α-Fe₂O₃. We now turn to the primary focus of this Article, the use of kinetic data such as that shown in Fig. 1a to provide insight into the mechanism of water oxidation on such electrodes. This analysis focuses on haematite alone, and in particular the origin of the third-order kinetics observed under 1 sun illumination conditions[16]. First, we consider the temperature dependence of the first- and third-order kinetics, as shown in the rate law analyses plotted in Fig. 2a.

The inset to this figure shows Arrhenius analyses of the data for the first- and third-order rate constants. We observe an activation energy (E_a) of 0.30 ± 0.05 eV for the first-order mechanism, consistent with that reported from transient absorption measurements under pulsed laser excitation[31]. More importantly, we observe that the third-order reaction mechanism has a very low activation energy, $E_a = 0.06 ± 0.02$ eV, indicating that at high hole densities, haematite is able to access a third-order reaction mechanism that essentially removes all significant activation energy barriers for the water oxidation reaction. Such a change in activation energy demonstrates that the haematite surface is indeed catalysing the water oxidation reaction at high surface hole densities, by lowering the activation barrier for this reaction to only 60 meV (see Supplementary Fig. 6 for an alternative E_a calculation).

Before turning to discuss possible reaction mechanisms compatible with such a low activation energy, we consider two further kinetic studies probing the reaction mechanism. Figure 2b plots the pH dependence of the first- and third-order water oxidation rate constants on haematite and Fig. 2c plots the kinetic isotope effect (KIE) of these rate constants for H_2O/D_2O exchange as a function of pH (Supplementary Fig. 7). It is apparent from Fig. 2b that both the first- and third-order rate constants are essentially pH-independent for pH values of up to 9.5, and then increase modestly (although not monotonically) for higher values of pH. The relatively weak pH dependence indicates that electrolyte hydroxides are not directly involved in the RDS of either reaction. The onset of a modest increase in k_{WO} above pH 9 coincides with the point of zero charge (PZC) of haematite (8–10)[32]. This suggests that the increase in k_{WO} above pH 9 is most likely associated with a change in the surface protonation of haematite. This also correlates with a change in the pH dependence of the photocurrent
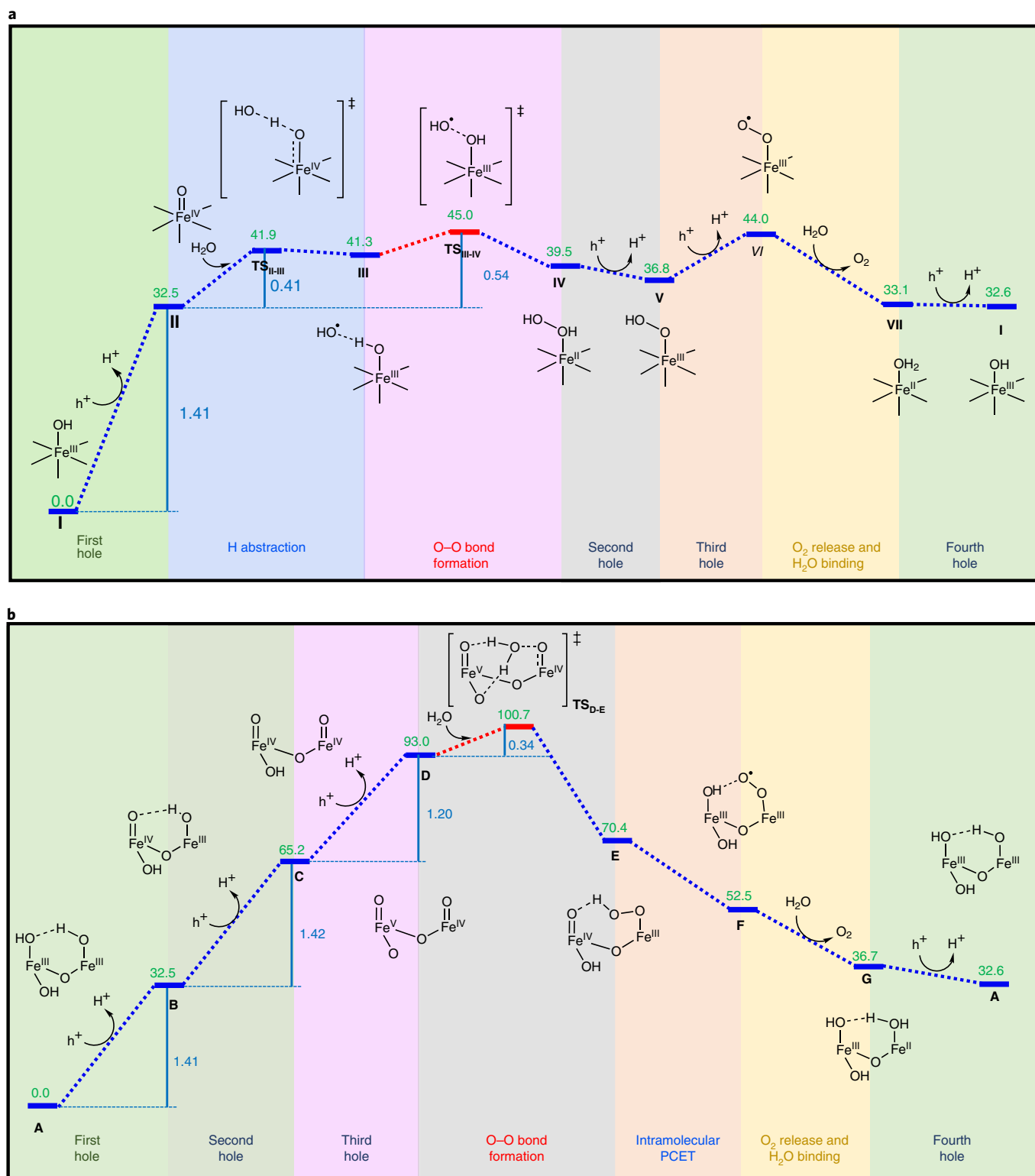
Fig. 3 | Potential water oxidation reaction mechanisms on α-Fe₂O₃. a,b, First- (**a**) and third-order (**b**) dependence kinetics, suggested by DFT calculations. Relative free energies are given in green in units of kcal mol⁻¹ and free energy changes are given in blue in units of eV. RDSs are shown in red. A photovoltage of 0.80 V is used for all oxidation steps. PCET: proton-coupled electron transfer.

onset potential from an ideal Nernstian 60 mV per pH at acidic/neutral pH to 100 mV per pH at alkaline pH (Supplementary Figs. 8 and 9).

From Fig. 2c, it is clear that the H/D KIE is small for the first-order rate constant at pH < 14 (KIE ≈ 1.1), indicating that O–H bond cleavage is not involved in the RDS of this reaction. On the
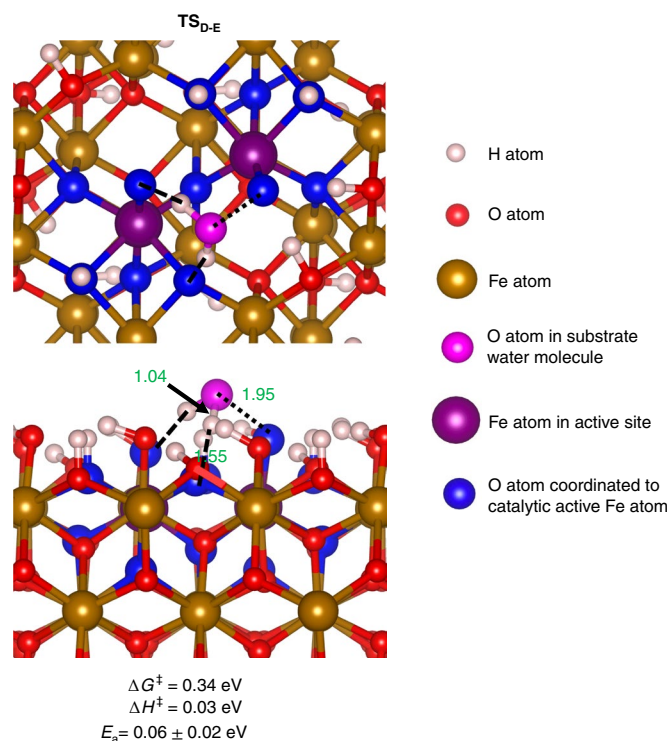
Fig. 4 | Potential transition state for the third-order kinetics on α-Fe₂O₃. Top and side views of optimized transition state (TS) structures with key bond lengths given in units of Å. Dashed lines indicate hydrogen bonds and dotted lines indicate partially formed bonds at transition states.

other hand, the third-order rate constant exhibits a modest secondary KIE effect, ~1.7 (expected KIE of 2.5, see DFT calculations below) from pH 7 to pH 11, decreasing to ~1.3 at more alkaline pH, which we discuss further in the following.

DFT calculations. DFT studies were undertaken to provide insight into the potential mechanisms of the observed first- and third-order water oxidation kinetics. We note that the extensive literature on theoretical studies on the water oxidation mechanism on haematite[33–38] have focused primarily on the thermodynamic aspect, with the kinetic data presented herein yet to be studied. We focus on the (110) surface of haematite, reported as the primary and most active facet for water oxidation, and the dominating facet of the photoelectrodes studied herein[39,40]. We employ a defect-free surface, consistent with our experimental observation of surface hole densities being much greater than typical surface defect densities. We focus on a reaction site based on a hydroxyl-terminated haematite (110) for which two neighbouring Fe(III)–OH groups form an Fe(OH)–O–Fe(OH) dimer in aqueous solutions (Figs. 3b and 4). Full details of the DFT calculations, including consideration of the haematite (110) surface/water interface, are given in the Supplementary Information.

We begin our discussion of the water oxidation mechanism corresponding to the observed first-order kinetics. Oxidation of a surface Fe(III)–OH leads to formation of Fe(IV)=O, requiring an energy of 1.41 eV and consistent with a recent study[30], which provided strong evidence for surface haematite holes comprising localized Fe(IV)=O species. Under low illumination, and therefore low hole densities, the Fe(IV)=O groups are isolated from each other. A potential pathway for water oxidation by such isolated surface holes is illustrated in Fig. 3a (see Supplementary Information for a detailed discussion). This mechanism is based on the oxidation of an incoming substrate H₂O molecule to form a hydroxyl radical, with the RDS of O–O

bond formation having an activation free energy of 0.54 eV and enthalpy of 0.26 eV. This activation enthalpy is in agreement with our experimental data for the first-order reaction. The H₂O₂ intermediate (**IV**) after the RDS could be further oxidized to produce O₂ (Fig. 3a) or released to the solution (Supplementary Fig. 11), with the former being thermodynamically more favourable. This mechanism is also consistent with our experimental data indicating only a weak pH dependence. Furthermore, the calculated H/D KIE associated with this mechanism is 1.03, again consistent with our experimental observation.

We now turn to consideration of the third-order reaction mechanism, which dominates under 1 sun operating conditions. We analysed successive (and potentially reversible) oxidations of an Fe(OH)–O–Fe(OH) dimer core by neighbouring haematite surface valence band holes (Figs. 3b and 5). Remarkably, the second and third oxidations of this dimer are thermodynamically similar to the first oxidation, with the third oxidation actually being the most facile. The second oxidation results in oxidation of the second Fe(III)–OH to Fe(IV)=O in the dimer, essentially corresponding to two nearest-neighbour haematite surface holes. The third oxidation oxidizes one of the Fe(IV)=O groups to Fe(V)=O while deprotonating a surface OH group coordinated to the Fe(V) centre. After three successive oxidations, the Fe dimer gains enough oxidation power to drive the nucleophilic attack of an incoming substrate water molecule (Fig. 4, **TS_{D-E}**), and subsequent O–O bond formation. This O–O bond formation is relatively facile, requiring an activation free energy of only 0.34 eV and enthalpy of 0.03 eV (Fig. 4), in good agreement with our experimental observed activation enthalpy (0.06 eV). This reaction mechanism is consistent with our measurement of a modest KIE. In particular, the RDS of O–O bond formation involves H atoms in the substrate water molecule (Fig. 4, **TS_{D-E}**), but does not involve O–H bond breaking. A similar KIE value has been reported for analysis of an analogous water oxidation mechanism on a ruthenium-based molecular catalyst[41]. The calculated H/D KIE with **TS_{D-E}** is 2.5, which is consistent with our experimentally observed KIE of ~1.7, indicating a modest secondary H/D KIE. Similarly, the RDS involves nucleophilic attack by a water molecule onto a Fe(IV)=O and does not directly involve hydroxide ions or proton release, consistent with the observed relatively weak pH dependence.

Mechanistic implications. The DFT calculations discussed above illustrate potential mechanisms for water oxidation consistent with our observed first and third reaction kinetics. We now consider the more general implications of these experimental and theoretical data, focusing on the key third-order reaction pathway, as illustrated in Fig. 5. A key element of this pathway is that three surface holes are in equilibrium with the triply oxidized cluster involved in the RDS. The accumulation of three oxidizing equivalents on a single cluster requires the lateral diffusion of surface holes, consistent with an analogous model previously proposed for Co₃O₄ (ref. [42]), until three holes accumulate together to enable O–O bond formation. The subsequent steps leading to O₂ release and H₂O binding, and fourth oxidation, are thermodynamically downhill with no activation barrier.

The similarity of the oxidation potentials for the first, second and third oxidations (redox levelling), as indicated by our DFT calculations, is analogous to that observed for the oxidations of the oxo-manganese complex of PS II[43,44] and for other catalytic systems such as RuO₂ (ref. [45]). As for PS II, an underlying redox levelling mechanism is probably essential to enable the accumulation of multiple oxidizing equivalents at multi-metallic reaction sites. In both cases, this ability to drive multiple oxidations of a single cluster with similar driving energies results primarily from the proton release associated with the first, second and third oxidations in our model, thus maintaining charge neutrality.
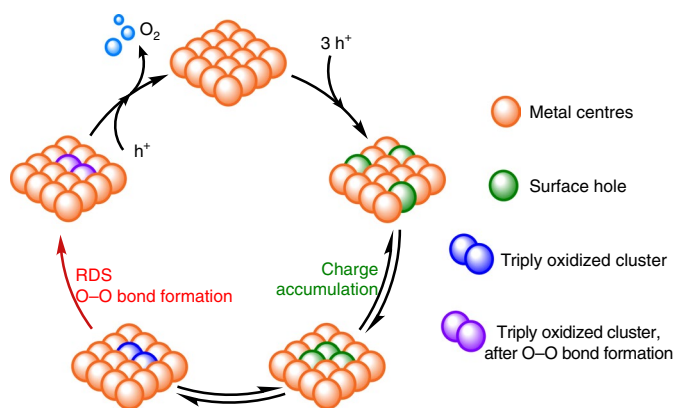
Fig. 5 | Schematic of the key steps in the proposed third-order water oxidation reaction. Equilibration between three surface holes and M(OH)–O–M(OH) sites is followed by O–O bond formation as the RDS, which is followed by a fourth oxidation and O_2 release.

Our DFT calculations indicate that the first, second and third oxidations of this cluster occur with similar oxidation potentials, without the need for consideration of any surface defects. This redox levelling can be attributed to proton release associated with each oxidation step, and is key to enabling the accumulation of three oxidizing equivalents on the cluster. Such redox levelling associated with proton coupled electron transfer is also observed in the multi-metal oxygen evolution centre of PS II.

Our observation of a modest acceleration of the rate constant at pH values greater than haematite's PZC, is consistent with the partial deprotonation of surface hydroxyls at a strongly alkaline pH. These deprotonated oxyl groups would provide effective proton transport channels to facilitate proton release from the oxidized cluster, thereby favouring the accumulation of multiple oxidation equivalents on a single dimer. Similarly, our observation of a modest increase in rate constant with VBE (Fig. 1c) could be explained by a shift of the equilibrium between three separated surface holes and the triply oxidized cluster towards the latter. This may also be associated with an increase in the surface hole reactivity for O–O bond formation.

The haematite photoelectrodes studied here are very distinct in terms of system architecture and material/molecular composition from the biological water oxidation enzyme PS II. For example, haematite undertakes the functions of both light absorber and catalyst, whereas in PS II these functions are separated between light-absorbing pigments and a metal cluster-based catalyst (the oxygen evolution complex (OEC)). However, it is interesting to note that some of the fundamental aspects of the third-order water oxidation reaction mechanism proposed herein for haematite (and potentially for other metal oxides, as discussed below) have parallels to mechanisms proposed for the OEC of PSII. Both the proposed oxyl–oxo coupling pathway[46,47] and the nucleophilic attack of a terminal oxyl radical by substrate water[48–52] for PS II require μ-oxo bridges linking the Mn metal centres in the OEC. These regulate the binding, deprotonation and oxidation of substrate water molecules as well as O–O bond formation processes, in ways analogous to those discussed herein for the haematite surface. For both systems, the thermodynamic coupling of oxidation and deprotonation events establishes a redox-levelling mechanism that enables low free energy pathways for the accumulation of multiple oxidizing equivalents. For both systems, the accumulation of multiple oxidizing equivalents in high-valent transition metal centres is necessary to induce deprotonation of water ligands and the formation of the reactive species responsible for O–O bond formation. On the other hand, clear differences are also apparent.

The reaction mechanism proposed herein for haematite proceeds via formation of a peroxo moiety, which contrasts to most models of water oxidation by PS II[43,47,52–55], but has been proposed for heterogeneous water oxidation on other metal oxides such as Co_3O_4 or IrO_2 (ref. [56]). It is also important to recognize that water oxidation on haematite (and the other oxides studied herein) proceeds with a slower turnover frequency and larger driving energy than for PS II. Clearly, the OEC of PS II is a far more complex and effective catalyst for water oxidation than the relatively unsophisticated metal oxide surfaces studied herein. As such, it is remarkable that parallels can be drawn between water oxidation by these two very distinct systems, indicating that studies of natural water oxidation may indeed provide guidelines to aid further development of artificial heterogeneous water oxidation catalysts.

Our observation of similar water oxidation rate laws for four different oxides suggests broadly similar reaction mechanisms for all four oxides. A full analysis of this issue is, however, beyond the scope of this study, with detailed specific reaction mechanisms likely to depend, for example, on the oxide surface facet and the nature of the surface holes. We note that the water oxidation models proposed herein for haematite show common features with analogous reaction mechanisms proposed for other metal oxides. In particular, Frei and others[57] observed distinct reaction intermediates for 'slow' and 'fast' water oxidation reactions on cobalt oxides, with proposed reaction mechanisms broadly consistent with the two first- and third-order reaction mechanisms proposed herein. From the plausible mechanisms of first- and third-order kinetics suggested by our DFT calculations, it is also possible that the participation of multiple nearby M–OH groups, as detailed in our third-order mechanism, is a common feature for efficient water oxidation on metal oxide surfaces. We note that both cobalt oxide and haematite have M(OH)–O–M(OH) sites, which can be oxidized by sequential proton-coupled oxidations to accumulate enough oxidation power. Similar M(OH)–O–M(OH) sites are not only present on most metal oxides, but also in recently developed highly active homogeneous Ir- and Fe-based catalysts[58,59] and in the $Fe(IV)_2$ diamond-core structure of carboxylate-rich, non-haem diiron enzyme systems[60–62], suggesting their importance for the development of efficient oxidation catalysts.

Data availability

The complete optical and electrochemical dataset is available at http://zenodo.org with the identifier 10.5281/zenodo.851635.

References

1. Zhu, S. & Wang, D. Photocatalysis: basic principles, diverse forms of implementations and emerging scientific opportunities. *Adv. Energy Mater.* **17**, 1700841 (2017).
2. Berardi, S. et al. Molecular artificial photosynthesis. *Chem. Soc. Rev.* **43**, 7501–7519 (2014).
3. Walter, M. G. et al. Solar water splitting cells. *Chem. Rev.* **110**, 6446–6473 (2010).
4. Lewis, N. S. & Nocera, D. G. Powering the planet: chemical challenges in solar energy utilization. *Proc. Natl Acad. Sci. USA* **103**, 15729–15735 (2006).
5. Sun, K. et al. A comparison of the chemical, optical and electrocatalytic properties of water-oxidation catalysts for use in integrated solar-fuel generators. *Energy Environ. Sci.* **10**, 987–1002 (2017).
6. McCrory, C. C. L., Jung, S., Peters, J. C. & Jaramillo, T. F. Benchmarking heterogeneous electrocatalysts for the oxygen evolution reaction. *J. Am. Chem. Soc.* **135**, 16977–16987 (2013).
7. Kärkäs, M. D. & Åkermark, B. Water oxidation using earth-abundant transition metal catalysts: opportunities and challenges. *Dalton Trans.* **45**, 14421–14461 (2016).
8. Blakemore, J. D., Crabtree, R. H. & Brudvig, G. W. Molecular catalysts for water oxidation. *Chem. Rev.* **115**, 12974–13005 (2015).
9. Llobet, A. *Molecular Water Oxidation Catalysis: A Key Topic for New Sustainable Energy Conversion Schemes* (2014, Wiley).

10. Dau, H. et al. The mechanism of water oxidation: from electrolysis via homogeneous to biological catalysis. *ChemCatChem* **2**, 724–761 (2010).

11. Shinagawa, T., Garcia-Esparza, A. T. & Takanabe, K. Insight on Tafel slopes from a microkinetic analysis of aqueous electrocatalysis for energy conversion. *Sci. Rep.* **5**, 13801 (2015).

12. Gerischer, H. The impact of semiconductors on the concepts of electrochemistry. *Electrochim. Acta* **35**, 1677–1699 (1990).

13. Francàs, L., Mesa, C. A., Pastor, E., Le Formal, F. & Durrant, J. R. in *Advances in Photoelectrochemical Water Splitting: Theory, Experiment and Systems Analysis* (eds Tilley, S. D., Lany, S. & van de Krol, R.) Ch. 5 (Royal Society of Chemistry, 2018).

14. Pastor, E. et al. Spectroelectrochemical analysis of the mechanism of (photo) electrochemical hydrogen evolution at a catalytic interface. *Nat. Commun.* **8**, 14280 (2017).

15. Mesa, C. A. et al. Kinetics of photoelectrochemical oxidation of methanol on hematite photoanodes. *J. Am. Chem. Soc.* **139**, 11537–11543 (2017).

16. Le Formal, F. et al. Rate law analysis of water oxidation on a hematite surface. *J. Am. Chem. Soc.* **137**, 6629–6637 (2015).

17. Ma, Y. et al. Rate law analysis of water oxidation and hole scavenging on a $BiVO_4$ photoanode. *ACS Energy Lett.* **1**, 618–623 (2016).

18. Kafizas, A. et al. Water oxidation kinetics of accumulated holes on the surface of a TiO_2 photoanode: a rate law analysis. *ACS Catal.* **7**, 4896–4903 (2017).

19. Pesci, F. M., Cowan, A. J., Alexander, B. D., Durrant, J. R. & Klug, D. R. Charge carrier dynamics on mesoporous WO_3 during water splitting. *J. Phys. Chem. Lett.* **2**, 1900–1903 (2011).

20. Barroso, M., Pendlebury, S. R., Cowan, A. J. & Durrant, J. R. Charge carrier trapping, recombination and transfer in hematite (α-Fe_2O_3) water splitting photoanodes. *Chem. Sci.* **4**, 2724–2734 (2013).

21. Roger, I., Shipman, M. A. & Symes, M. D. Earth-abundant catalysts for electrochemical and photoelectrochemical water splitting. *Nat. Rev. Chem.* **1**, 0003 (2017).

22. Rosser, T. E., Gross, M. A., Lai, Y.-H. & Reisner, E. Precious-metal free photoelectrochemical water splitting with immobilised molecular Ni and Fe redox catalysts. *Chem. Sci.* **7**, 4024–4035 (2016).

23. Zhang, Y. et al. Rate-limiting O−O bond formation pathways for water oxidation on hematite photoanode. *J. Am. Chem. Soc.* **140**, 3264–3269 (2018).

24. Schulze, M., Kunz, V., Frischmann, P. D. & Würthner, F. A supramolecular ruthenium macrocycle with high catalytic activity for water oxidation that mechanistically mimics photosystem II. *Nat. Chem.* **8**, 576–583 (2016).

25. Kafizas, A. et al. Optimizing the activity of nanoneedle structured WO_3 photoanodes for solar water splitting: direct synthesis via chemical vapor deposition. *J. Phys. Chem. C* **121**, 5983–5993 (2017).

26. Cowan, A. J., Leng, W., Barnes, P. R. F., Klug, D. R. & Durrant, J. R. Charge carrier separation in nanostructured TiO_2 photoelectrodes for water splitting. *Phys. Chem. Chem. Phys.* **15**, 8772 (2013).

27. Ma, Y., Le Formal, F., Kafizas, A., Pendlebury, S. R. & Durrant, J. R. Efficient suppression of back electron/hole recombination in cobalt phosphate surface-modified undoped bismuth vanadate photoanodes. *J. Mater. Chem. A* **3**, 20649–20657 (2015).

28. Wang, X. H. et al. Pyrogenic iron(III)-doped TiO_2 nanopowders synthesized in RF thermal plasma: phase formation, defect structure, band gap and magnetic properties. *J. Am. Chem. Soc.* **127**, 10982–10990 (2005).

29. Wahlström, E. et al. Bonding of gold nanoclusters to oxygen vacancies on rutile TiO_2 (110). *Phys. Rev. Lett.* **90**, 026101 (2003).

30. Zandi, O. & Hamann, T. W. Determination of photoelectrochemical water oxidation intermediates on haematite electrode surfaces using operando infrared spectroscopy. *Nat. Chem.* **8**, 778–783 (2016).

31. Cowan, A. J. et al. Activation energies for the rate-limiting step in water photooxidation by nanostructured α-Fe_2O_3 and TiO_2. *J. Am. Chem. Soc.* **133**, 10134–10140 (2011).

32. Kosmulski, M. pH-dependent surface charging and points of zero charge. IV. Update and new approach. *J. Colloid Interface Sci.* **337**, 439–448 (2009).

33. Aharon, E. & Toroker, M. C. The effect of covering Fe_2O_3 with a Ga_2O_3 overlayer on water oxidation catalysis. *Catal. Lett.* **147**, 2077–2082 (2017).

34. Yatom, N., Elbaz, Y., Navon, S. & Caspary Toroker, M. Identifying the bottleneck of water oxidation by ab initio analysis of in situ optical absorbance spectrum. *Phys. Chem. Chem. Phys.* **19**, 17278–17286 (2017).

35. Seriani, N. Ab initio simulations of water splitting on hematite. *J. Phys. Condens. Matter* **29**, 463002 (2017).

36. Grave, D. A., Yatom, N., Ellis, D. S., Toroker, M. C. & Rothschild, A. The 'rust' challenge: on the correlations between electronic structure, excited state dynamics and photoelectrochemical performance of hematite photoanodes for solar water splitting. *Adv. Mater.* **30**, 1706577 (2018).

37. Nguyen, M.-T., Seriani, N. & Gebauer, R. Back cover: defective α-Fe_2O_3 (0001): an ab initio study. *ChemPhysChem* **15**, 3136–3136 (2014).

38. Zhang, X., Klaver, P., Van Santen, R., Van Der Sanden, M. C. M. & Bieberle-Hütter, A. Oxygen evolution at hematite surfaces: the impact of structure and oxygen vacancies on lowering the overpotential. *J. Phys. Chem. C* **120**, 18201–18208 (2016).

39. Kay, A., Cesar, I. & Grätzel, M. New benchmark for water photooxidation by nanostructured α-Fe_2O_3 films. *J. Am. Chem. Soc.* **128**, 15714–15721 (2006).

40. Cornuz, M., Grätzel, M. & Sivula, K. Preferential orientation in hematite films for solar hydrogen production via water splitting. *Chem. Vap. Depos.* **16**, 291–295 (2010).

41. Yamada, H., Siems, W. F., Koike, T. & Hurst, J. K. Mechanisms of water oxidation catalyzed by the cis,cis-[(bpy)$_2$Ru(OH$_2$)]$_2$O^{4+} ion. *J. Am. Chem. Soc.* **126**, 9786–9795 (2004).

42. Pham, H. H., Cheng, M.-J., Frei, H. & Wang, L.-W. Surface proton hopping and fast-kinetics pathway of water oxidation on Co_3O_4 (001) surface. *ACS Catal.* **6**, 5610–5617 (2016).

43. Askerka, M., Brudvig, G. W. & Batista, V. S. The O_2-evolving complex of photosystem II: recent insights from quantum mechanics/molecular mechanics (QM/MM), extended X-ray absorption fine structure (EXAFS), and femtosecond X-ray crystallography data. *Acc. Chem. Res.* **50**, 41–48 (2017).

44. Amin, M. et al. Proton-coupled electron transfer during the *S*-state transitions of the oxygen-evolving complex of photosystem II. *J. Phys. Chem. B* **119**, 7366–7377 (2015).

45. Rossmeisl, J. et al. Electrolysis of water on oxide surfaces. *J. Electroanal. Chem.* **607**, 83–89 (2007).

46. Siegbahn, P. E. M. O–O bond formation in the S_4 state of the oxygen-evolving complex in photosystem II. *Eur. J. Chem. A* **12**, 9217–9227 (2006).

47. Siegbahn, P. E. M. Water oxidation mechanism in photosystem II, including oxidations, proton release pathways, O–O bond formation and O_2 release. *Biochim. Biophys. Acta* **1827**, 1003–1019 (2013).

48. Pecoraro, V. L., Baldwin, M. J., Caudle, M. T., Hsieh, W.-Y. & Law, N. A. A proposal for water oxidation in photosystem II. *Pure Appl. Chem.* **70**, 925–929 (1998).

49. Vrettos, J. S., Limburg, J. & Brudvig, G. W. Mechanism of photosynthetic water oxidation: combining biophysical studies of photosystem II with inorganic model chemistry. *Biochim. Biophys. Acta* **1503**, 229–245 (2001).

50. Sproviero, E. M., Gascó, J. A., Mcevoy, J. P., Brudvig, G. W. & Batista, V. S. Quantum mechanics/molecular mechanics study of the catalytic cycle of water splitting in photosystem II. *J. Am. Chem. Soc.* **130**, 3428–3442 (2008).

51. Barber, J. A mechanism for water splitting and oxygen production in photosynthesis. *Nat. Plants* **3**, 17041 (2017).

52. Barber, J. Photosystem II: the water splitting enzyme of photosynthesis and the origin of oxygen in our atmosphere. *Q. Rev. Biophys.* **49**, e14 (2017).

53. Li, X. & Siegbahn, P. E. M. Water oxidation for simplified models of the oxygen-evolving complex in photosystem II. *Chem. A Eur. J.* **21**, 18821–18827 (2015).

54. Klauss, A., Haumann, M. & Dau, H. Seven steps of alternating electron and proton transfer in photosystem II water oxidation traced by time-resolved photothermal beam deflection at improved sensitivity. *J. Phys. Chem. B* **119**, 2677–2689 (2015).

55. Vinyard, D. J. & Brudvig, G. W. Progress toward a molecular mechanism of water oxidation in photosystem II. *Annu. Rev. Phys. Chem.* **68**, 101–116 (2017).

56. Zhang, M. & Frei, H. Water oxidation mechanisms of metal oxide catalysts by vibrational spectroscopy of transient intermediates. *Annu. Rev. Phys. Chem.* **68**, 209–231 (2017).

57. Zhang, M., De Respinis, M. & Frei, H. Time-resolved observations of water oxidation intermediates on a cobalt oxide nanoparticle catalyst. *Nat. Chem.* **6**, 362–367 (2014).

58. Yang, K. R. et al. Solution structures of highly active molecular Ir water-oxidation catalysts from density functional theory combined with high-energy X-ray scattering and EXAFS spectroscopy. *J. Am. Chem. Soc.* **138**, 5511–5514 (2016).

59. Gamba, I., Codolà, Z., Lloret-Fillol, J. & Costas, M. Making and breaking of the O–O bond at iron complexes. *Coord. Chem. Rev.* **334**, 2–24 (2017).

60. Tinberg, C. E. & Lippard, S. J. Dioxygen activation in soluble methane monooxygenase. *Acc. Chem. Res.* **280**, 280–288 (2011).

61. Shu, L. et al. An $Fe_2^{IV}O_2$ diamond core structure for the key intermediate Q of methane monooxygenase. *Science* **275**, 515–518 (1997).

62. Friedle, S., Reisner, E. & Lippard, S. J. Current challenges of modeling diiron enzyme active sites for dioxygen activation by biomimetic synthetic complexes. *Chem. Soc. Rev.* **39**, 2768–2779 (2010).

Acknowledgements

Author contributions

C.A.M. and L.F. contributed equally to this work. All authors discussed the results and commented on and revised the manuscript. C.A.M., L.F. and J.R.D. conceived and designed the experiments. K.R.Y., P.G. and V.S.B. contributed the DFT work. E.P., Y.M., A.K., T.E.R., M.T.M., E.R. and M.G. contributed materials and data.

Competing interests

The authors declare no competing interests.

Additional information

Supplementary information is available for this paper at https://doi.org/10.1038/s41557-019-0347-1.

Correspondence and requests for materials should be addressed to V.S.B. or J.R.D.

Reprints and permissions information is available at www.nature.com/reprints.

Publisher's note Springer Nature remains neutral with regard to jurisdictional claims in published maps and institutional affiliations.